Computational Insights into Water Oxidation Mechanisms on Rutile SnO$_2$ (110) that Form Ozone

Lingyan Zhao,[†] Rayan Alaufey,[‡] Qin Wu,[¶] Maureen Tang,[‡] and John A. Keith[*,†]

[†]*Department of Chemical and Petroleum Engineering, University of Pittsburgh, 3700 O'Hara Street, Pittsburgh, PA 15261*

[‡]*Department of Chemical and Biological Engineering, Drexel University, 3141 Chestnut St, Philadelphia, PA 19104*

[¶]*Center for Functional Nanomaterials, Brookhaven National Laboratory, Upton, NY, 11973*

E-mail: jakeith@pitt.edu

Abstract

Electrochemical ozone production (EOP) is intriguing as a sustainable route for generating powerful chemical oxidants and disinfectants, but atomic scale details of EOP mechanisms on nickel and antimony doped SnO$_2$ (NATO) electrocatalysts have been unclear. We used computational quantum chemistry to evaluate the thermodynamic feasibility of six-electron water oxidation steps based on 1) the adsorbate evolving mechanism (AEM) and the lattice oxygen mechanism (LOM). This work provides atomic scale insights into the atomic scale nature of tin oxide-based electrocatalysts under highly oxidizing potentials and how and why dopants would influence EOP catalysis on NATO. Importantly, we identify that EOP adsorbates are significantly stabilized by explicit hydrogen bonding networks that arise from H* and OH* intermediates that

1

form from dissociated water molecules, likely over the entire SnO_2 surface. The disso-
ciated water network is essential to developing computational catalysis model for EOP
that is qualitatively consistent with experimental observations.

Introduction

Ozone (O_3) is a powerful chemical oxidant that may someday become a large-scale sustain-
able alternative for chlorine disinfectants,[1,2] but the current conventional process for ozone
production is the cold corona discharge method,[3] which applies high voltages on dry air or
oxygen gas. The cold corona discharge method brings several intrinsic inefficiencies due to
heat losses while forming ozone and transport limitations when introducing gaseous ozone
into contaminated water for disinfection.

Alternatively, electrochemical ozone production (EOP) might be a route to avoid these
inefficiencies by generating solvated ozone directly in contaminated water if a suitably active
and stable electrocatalyst were found.[4–6] The EOP is a six-electron process that produces
ozone from water ($3\,H_2O \rightarrow\ O_3 + 6\,H^+ + 6\,e^-$, $E° = 1.51$ V). Key challenges toward
its development include the fact that catalysts must be selective for EOP rather than the
four-electron oxygen evolution reaction (OER: $2\,H_2O \rightarrow\ O_2 + 4\,H^+ + 4\,e^-$, $E° = 1.23$
V), and most EOP catalysts bring high anodic overpotentials on the order of 1 V that
necessitate the use of electrodes stable at highly oxidizing potentials. We posit that a better
understanding of atomic scale reaction mechanisms would contribute to better engineered
EOP electrocatalysts.

Atomic scale OER mechanisms have already received significant attention.[7–11] Notably,
Zagalskaya and Alexandrov have investigated two distinguishable mechanisms that warrant
consideration for water oxidation processes: the adsorbate evolving mechanism (AEM) and
the lattice oxygen mechanism (LOM).[12] The AEM assumes that the metal ions in an oxide
act as active sites for catalysis, and O_2 is evolved via reactions of conventional adsorbed
intermediates (e.g. O* and OH*) on the electrode surface. In the LOM, O_2 is evolved

2

from oxygens from the oxide lattice. For either process to be catalytic, oxygens on the surface and/or in the electrode would be readily replenished with oxygens from water in the electrolyte.

Compared to the OER, there have been much fewer reports on EOP mechanisms.[13–17] Studies have reported a variety of stable electrode materials, including boron-doped diamond (BDD),[18,19] PbO_2[17,20,21] and doped SnO_2.[22,23] As an example of insightful experimental and computational collaborations for EOP processes, Jiang *et al.* investigated AEM and LOM mechanisms for EOP on PbO_2 electrocatalysts. Their study used water with ^{18}O isotope labels, and differential electrochemical mass spectrometry results indicated that the majority of the oxygen in O_3 came from the PbO_2 lattice.[17] Furthermore, their Kohn-Sham density functional theory (DFT) calculations supported the feasibility of oxygen hopping mechanisms where lattice oxygens could migrate to the surface and directly couple to form O_3. This work converges to the conclusion that the LOM is the dominant EOP pathway on PbO_2, but comparable extensive experimental and computational collaborations have not been carried out for another oxide catalysts.

Pure SnO_2 cannot catalyze EOP, but nickel and antimony doped tin oxide (NATO, Ni-Sb-SnO_2) are among the most studied EOP catalysts for this reaction.[24–28] Seminal work by Christensen *et al.* reported that NATO electrodes had faradaic efficiencies of approximately 20%. Sb has been observed to improve electronic conductivity of the tin oxide[29] while Ni was believed to improve EOP catalysis, allegedly by introducing oxygen vacancies.[14] We previously reported that adding Gd to NATO (i.e. Ni_x-$Gd_{(1-x)}$-Sb-SnO_2) allows even higher EOP faradaic efficiencies up to around 64%.[23] In that study, we also hypothesized that the precise role of dopants in SnO_2 electrodes would be identified with computational catalysis investigations of the LOM, AEM, and solution phase reactions that may involve radical oxygen species (ROS). Again, since the main role of Sb has been assumed to provide mechanical stability and improved electronic conductivity in tin oxide,[27,30] we presumed that the beneficial roles of Ni (and Gd) dopant effects would be more likely observed using

3

computational catalysis modeling. In fact, our calculations showed that Ni-doping resulted in significantly *higher* theoretical overpotentials while Gd-doping resulted in a negligible difference to pure SnO_2. This indicated that our model contained a significant unphysical discrepancy that made computational results inconsistent with experimental observations. At the time, we reasoned that this inconsistency was due to using too small a surface unit cell, insufficient modeling of coverage effects, and/or an inadequate modeling of solvation on the interface. Those aspects are now addressed in this study.

This report shows an improved elucidation into the role of Ni in NATO-based EOP catalysts. We have used larger surface unit cells that allow us to consider complex surface structures with explicit solvent interactions that have not yet been reported in computational studies of EOP. From this modeling, several important insights arise including 1) PbO_2 and doped SnO_2 likely have different EOP mechanisms because they have significantly different oxygen vacancy formation energies, 2) explicit water structures play a key role in thermodynamically stabilizing EOP intermediates that are affected by Ni-doping, and this result explains why prior computational modeling had been inconsistent with experiment.

Computational Methods

Electronic structure calculations

Our prior work that used a 2×1 $SnO_2(110)$ surface slab model to model EOP steps,[23] but this present study used a 2×2 $SnO_2(110)$ surface slab model to more physically model more adsorbate configurations that would be relevant for the AEM and LOM. This larger unit cell was also used by Li *et al.*[31] to address EOP mechanisms on PbO_2. We applied Kohn–Sham density functional theory (DFT) on the slab model using the Vienna Ab initio Simulation Package (VASP) code version 5.4.4 using the GPU.[32–35] Electronic energies were calculated using the Perdew-Burke-Ernzerhof (PBE) exchange-correlation functional using Projector Augmented Wave (PAW) pseudopotentials[36,37] with a plane wave energy cutoff

4

of 450 eV. Spin polarization was used to model the triplet state of O_2 molecule. A 4×8×1 Monkhorst-Pack grid sampling of k-points was used for all surface calculations. The atoms in the bottom two layers of the slab were fixed while the atoms in the upper two layers and adsorbates were allowed to relax until the energy change between steps was within 0.1 meV using the conjugate gradient algorithm.
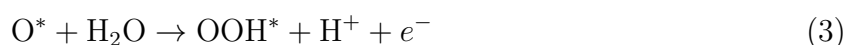
We introduced dopants into the surface by substituting a top layer Sn atom with either a Ni (or a Gd atom, as reported in the Supporting Information). Note that in this unit cell, the theoretical dopant concentration is 3%, while the experimental dopant percentage is 0.1%. The detailed discussion of dopant modeling is reported in the Supporting Information. Since modeling smaller dopant concentrations would require a substantially larger unit cell, we followed our previous work[38] where we assumed that the dopant's effect on influencing adsorbate binding energies will be local, and whatever effect the dopant has will be maximized when it is directly adjacent to the adsorbate. Thus, for each adsorbate structure, we modeled a variety of local dopant positions to find the structure with the lowest electronic energy, and that was the structure used in our thermodynamic analysis. With this assumption, we expect that our results would reflect a qualitative upper limit of the actual dopant effect. To obtain more statistically significant data that would better correlate with experiment, one would ideally model several different ensembles of adsorbates and dopant configurations on different surface facets using Monte Carlo algorithms (*e.g.* as done in Ref.[39]), but this was expected to be too costly for these systems, and so simplifying approximations were made instead.

For all slab model structures, we approximated the absolute free energy of each system as the DFT electronic energy as calculated using VASP and then assumed that zero-point vibrational and thermal contributions were negligible. For the energies of gas phase water and ozone molecules that are used in conjuction with slab calculations, we used DFT electronic energies as calculated using VASP and then added additional thermodynamic entropy contributions using values from the NIST webbook.[40] For the energy of solvated water in

conjuction with slab calculations, we used the gas phase DFT energy and added the solvation energy contribution that includes appropriate standard state corrections following earlier work.[41] These data were considered alongside other data we previously reported for solution phase ROS molecules that were calculated using high-level *ab initio* thermochemical data with mixed implicit and explicit solvation models.[23]

Models

The CHE model[42] and electrochemical surface phase diagrams (summarized in Ref.[43]) were used to analyze reaction intermediates at different applied potentials. To describe the EOP process, we start from the conventional scheme of equations used for CHE modeling of the OER (Eq. 1 − 4)[11] and then extend it to include two more reactions so that we can consider a total of six proton and electron transfers away from three reactant water molecules (Eq. 5 − 6).

$$H_2O + * \rightarrow OH^* + H^+ + e^- \tag{1}$$

$$OH^* \rightarrow O^* + H^+ + e^- \tag{2}$$

$$O^* + H_2O \rightarrow OOH^* + H^+ + e^- \tag{3}$$

$$OOH^* \rightarrow O_2^* + H^+ + e^- \tag{4}$$

$$O_2^* + H_2O \rightarrow HO_3^* + H^+ + e^- \tag{5}$$

$$HO_3^* \rightarrow O_3 + * + H^+ + e^- \tag{6}$$

The net reaction for Eq. 1 − 6 is: 3 $H_2O \rightarrow O_3$ + 6H^+ + 6 e^-. The * in the above equations denotes a surface adsorption site, so the O* reflects an O atom on the surface. Note that Eqs. 1 − 6 could be valid for either an AEM or LOM, but the difference would reflect whether the oxygen atoms arise from the water electrolyte (in the AEM) or via the

generation of oxygen vacancies in the oxide lattice (in the LOM). The CHE model treats the energy of a proton and electron transfer is accounted as:

$$\mu_{\text{H}^+} + \mu_{e^-} = \frac{1}{2}G_{\text{H}_2} \tag{7}$$

An applied potential (or pH effect) can then be considered as a perturbation to the above expression. To model an applied potential, a more positive potential relative to the SHE scale, U_{SHE}, would shift reaction energetics of reaction intermediates by $-eU$. To model an applied potential and pH effects, one would use the following expression:

$$\mu_{\text{H}^+} + \mu_{e^-} = \frac{1}{2}\mu_{\text{H}_2} - e\text{U}_{\text{SHE}} - 0.059 \times \text{pH} \tag{8}$$

Using atomistic thermodynamics schemes,[44–46] the chemical potential of an oxygen vacancy can be represented as:

$$\mu_{\text{O}_{\text{vac}}} = \mu_{\text{H}_2\text{O}} - \mu_{\text{H}_2} + 2 \times e\text{U}_{\text{SHE}} + 2 \times 0.059 \times \text{pH} \tag{9}$$

Environmental effects may also impact the activity of water, and these can be considered with the following expression:

$$\mu_{\text{H}_2\text{O}} = G_{\text{H}_2\text{O}} + \Delta\mu_{\text{H}_2\text{O}} \tag{10}$$

where $\Delta\mu_{\text{H}_2\text{O}}$ represents a deviation of the chemical potential of water in its standard state. In environments when water is more stabilized than in bulk solution in its standard state ($\Delta\mu_{\text{H}_2\text{O}} < 0$, and in environments when water is less stabilized ($\Delta\mu_{\text{H}_2\text{O}} > 0$).

To summarize, the change in reaction free energy for an arbitrary electrochemical process that accounts for environmental effects due to applied potential, pH, and/or water activity

7

would be represented as:

$$\Delta G_{\mathrm{rxn}} = G_{\mathrm{ads}} - G_{\mathrm{slab}}$$
$$+ n(0.5\mathrm{H}_2 - e\mathrm{U} - 0.059 \text{ pH})$$
$$- a(G_{\mathrm{H_2O}} + \Delta\mu_{\mathrm{H_2O}})$$
$$+ b(G_{\mathrm{H_2O}} + \Delta\mu_{\mathrm{H_2O}} - \mu_{\mathrm{H_2}} + 2e\mathrm{U} + 2 \times 0.059 \text{ pH}) \tag{11}$$

where G_{ads} is free energy of an intermediate state, G_{slab} is the free energy of the pristine SnO_2 slab, and n, a, and b are the numbers of proton and electron transferred, the number of water, and the number of O vacancy defects that need to be added or subtracted from the reference slab to create the intermediate state, respectively. Eq. 11 is used to generate all electrochemical phase diagrams used in this study. Since experimental conditions operated at acidic conditions (at approximately pH 0), we neglected the pH contribution.

Results and Discussion

LOM consideration and the role of explicit water coadsorption

As mentioned in the introduction, computational data from our previous study[23] was not consistent with experimental observations that Ni doping improves EOP catalysis. We now report results for the LOM on $SnO_2(110)$ using calculations with a larger unit cell and with and without explicit water coadsorbates. We consider the energetics of an oxygen migration to the surface that creates a vacancy on a clean $SnO_2(110)$ surface in the presence of different adsorbates including one or more explicit water molecules (see Figure 1).
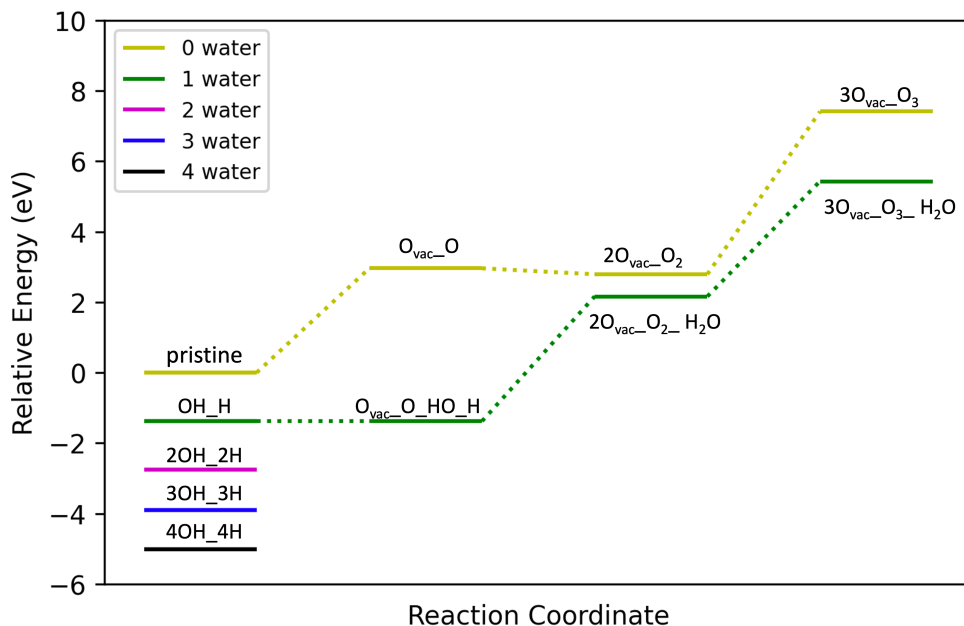
8

Figure 1: A calculated free energy diagram showing relative energetics for LOM processes and the effect of explicit water on the surface. The x-axis signifies a sequence of chemical steps toward the production of ozone. Yellow line: LOM steps with no coadsorbed water. Green line: LOM steps with one explicit water (occupying the oxygen vacancy site). The purple, blue, and black lines show the relative energies of two, three, and four dissociated waters adsorbed on surface, and calculations for additional vacancies were not performed. Water molecules are found to significantly stabilize the adsorbate intermediates and fill surface oxygen vacancies.

The steps corresponding to the yellow line start with a bridging oxygen atom on $SnO_2(110)$ first migrating onto an Sn top site, and this results in an oxygen vacancy on the surface: O_{vac}_O. This step is calculated to be +2.96 eV uphill. The top-site oxygen adsorbate then binds with another bridging oxygen to form an O_2 adsorbate ($2O_{vac}\_O_2$) which is slightly downhill in energy by 0.20 eV relative to the O_{vac}_O state. The O_2 intermediate can then bind with another in-plane oxygen which leads to a state that is 4.65 eV higher than the $2O_{vac}\_O_2$ state. We note that our new oxygen vacancy formation energy on the 2×2 $SnO_2(110)$ surface (+2.17 eV) is reasonably consistent with our prior calculations on the 2×1 unit cell (+2.30 eV)[23] as well as other expectedly reliable literature values that range from $2.0 - 2.3$ eV.[46]

We then modeled an analogous mechanism that now involved a coadsorbed water molecule

9

(green line in Figure 1). First, a single water will bind onto $SnO_2(110)$ with an energy of 1.38 eV after dissociating into O* and OH* intermediates. This observation is consistent with previous calculations by Santarossa et al.[47] who used Born-Oppenheimer molecular dynamics studies of a water molecule on the $SnO_2(110)$ surface. By comparing the energetics shown in the first step of the yellow line pathway and the first step of the green line pathway, we observe that there is a significant driving force (4.34 eV) to refill the oxygen vacancy with an explicit water. Furthermore, a single water molecule will bring 0.63 eV, and 1.97 eV of stabilization to O_2* next to two O-vacancies (one of which is filled with the water), and O_3* next to three O-vacancies (one of which is filled with the water), respectively. The net effect is that one explicit water causes the reaction energy for O_2 forming O_3 from a lattic oxygen atom to decrease from +4.61 eV to +3.27 eV.

When a second water is added to the surface, the second water dissociates leaving a surface covered with dissociated water molecules (the pink line). The adsorption energies of two dissociated waters on the surface of $SnO_2(110)$ is −2.78 eV, and this was approximately −0.85 eV more stable than other structures that had one dissociated water and one intact water or two intact waters. When three and four waters bind to the surface, all are found to dissociate and the binding energy is −3.90 eV and −5.02 eV, respectively. This result shows that on $SnO_2(110)$ surfaces, the adsorption energy of water exhibits a nearly linear relationship until the surface coverage is approximately 75% percent, indicating little steric crowding of dissociated waters until coverages above 75% are achieved.

This also indicates that the lowest energy facet of tin oxide under ambient electrochemical conditions are highly unlikely to resemble a clean surface, but they will rather be a surface covered with OH* and H* intermediates, which in turn would also likely interact with non-adsorbed water molecules. Unfortunately, since the $SnO_2(110)$ surface is not amenable to a straightforward hexagonal ice layer structure that is often used to model solvated (111) facets of fcc metals, the explicit water layer would need to be generated through numerous iterative DFT calculations (as done more extensively in Ref.[48]) or by using costly reactive

dynamics simulations that involve additional molecules. The Supporting Information provides a computational catalysis analysis of AEM steps on the larger 2×2 unit cell where intermediates can be impacted by either Ni and Gd dopants as well as the presence of up to one explicit water molecule. Those computational results show that even on the larger surface model, a simplistic CHE model for the EOP mechanism is not sufficient to show that experimentally known dopants like Ni and Gd would bring about lower overpotentials.

Electrochemical phase diagrams accounting for multiple waters and dopants

Although a thorough assessment of reaction structures involving EOP intermediates with full coverage of co-adsorbed and non-coadsorbed water is not possible at this time, we posited that calculations involving a limited number of explicit hydrogen bonding interactions on the surface might be useful for insights into EOP mechanisms. As an initial assessment of which surface adsorbate structures are the most energetically viable at different electrode potentials, we compiled 48 different geometrically relaxed structures on the undoped and clean slab systems that involved up to four oxygen atoms and four hydrogen atoms, all into an electrochemical atomistic thermodynamics model as outlined in Ref.[43] In this way, we could model the putative intermediates for the AEM and LOM pathways: OH*, O*, OOH*, O_2*, O_3H*, and O_3*, all in the presence of different numbers of hydrogens and oxygens that would arise from coadsorbed species.

We then categorized all of the surface structures based on the number of oxygen and hydrogen atoms they contained, and then we identified the lowest energy structure for each category (detailed in Supporting Information) and illustrated it using figures to the right of the phase diagram. For the doped cases, we considered different configurations where one of the Sn atoms in the top layer of the surface was substituted with the dopant, and the lowest energy structure was used in the phase diagram. The x-axis shows a change in chemical potential of bulk water. The vertical dashed line is set to $\Delta \mu_{H_2O} = 0$ *i.e.* the state obtained

11

https://doi.org/10.26434/chemrxiv-2023-w19vx **ORCID:** https://orcid.org/0000-0002-6583-6322 Content not peer-reviewed by ChemRxiv. **License:** CC BY-NC-ND 4.0

directly from the DFT calculations with no other thermochemical approximations. Relative energy differences between structures are tabulated in supporting information.

Note that our model assumes that all oxygen atoms are indistinguishable and additional oxygen atoms can be readily obtained from solution phase water. In this way, these phase diagrams will identify key reaction intermediates that would be viable for either AEM or LOM processes. For example, Figure 2 shows the most stable structures at pH 0 at the different applied potentials and chemical potentials of water. The region denoted with the label of 20 shows that the most stable surface structure in the range of applied potentials higher than 2.22 V is O_3* co-adsorbed with dissociated water. The diagram also shows that the thermodynamic limiting potential of the pristine surface is 2.22 V, which is in accordance with our calculations reported in Table S1. The diagram also shows that at almost all conditions (except those denoted using label 2, where chemical potentials of water are more negative than -0.9 eV and applied potentials are less than 1 V), at least one water molecule will co-adsorb onto the surface in a dissociative way. In fact, based on Figure 1, considerations of more waters would presumably allow up to a full surface coverage of water molecules to adsorb. However, it is also unclear if additional coadsorbed waters at other surface sites would change qualitative aspects of this current analysis since 1) we observed the roughly linear correspondence seqential binding energies of water on this surface which indicates low levels of interactions between adsorbates bound to the different Sn sites, and 2) we anticipate a degree of error cancellation when comparing relative energies. Our present model indicates that the most thermodynamically stable surface structure at high applied potentials prior to forming ozone is O_2* with two coadsorbed water molecules that are dissociated across multiple sites. Lastly, our figure shows that the EOP potential would not be significantly impacted by the chemical potential of water because structure 18 (which represents O_2* co-adsorbed with two water molecules) has the same number of oxygen atoms as structure 20 (which represents O_3* co-adsorbed with one explicit water). In fact, we suspect the boundary between species 18 and 20 would be a diagonal line if we were able to

12

model each surface with a fully saturated layer of water since species 18 has one vacant Sn site while species 20 has two vacant sites.
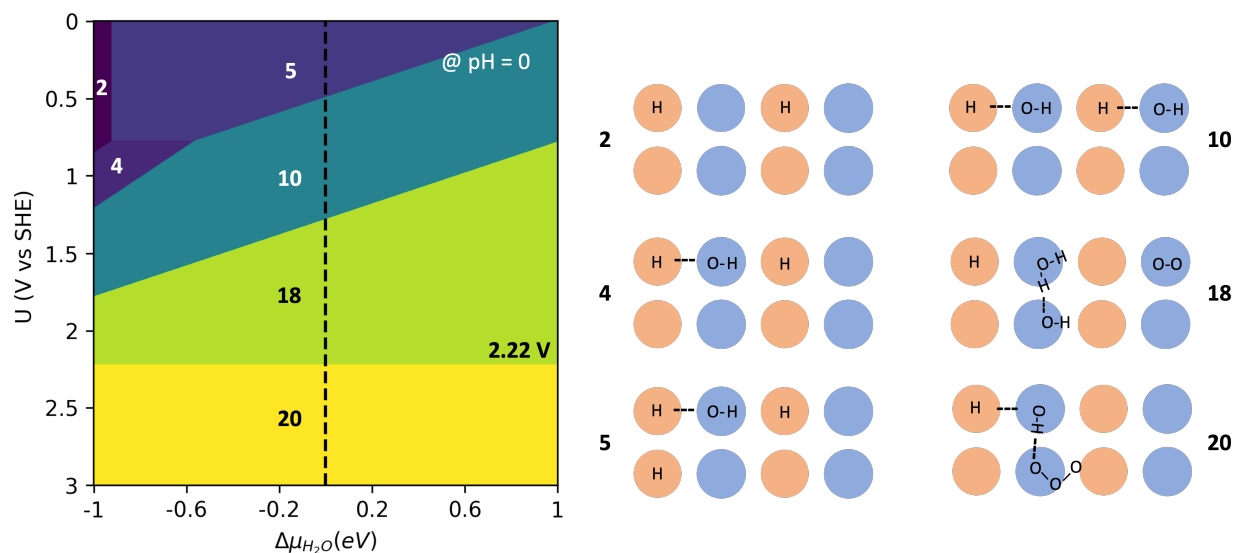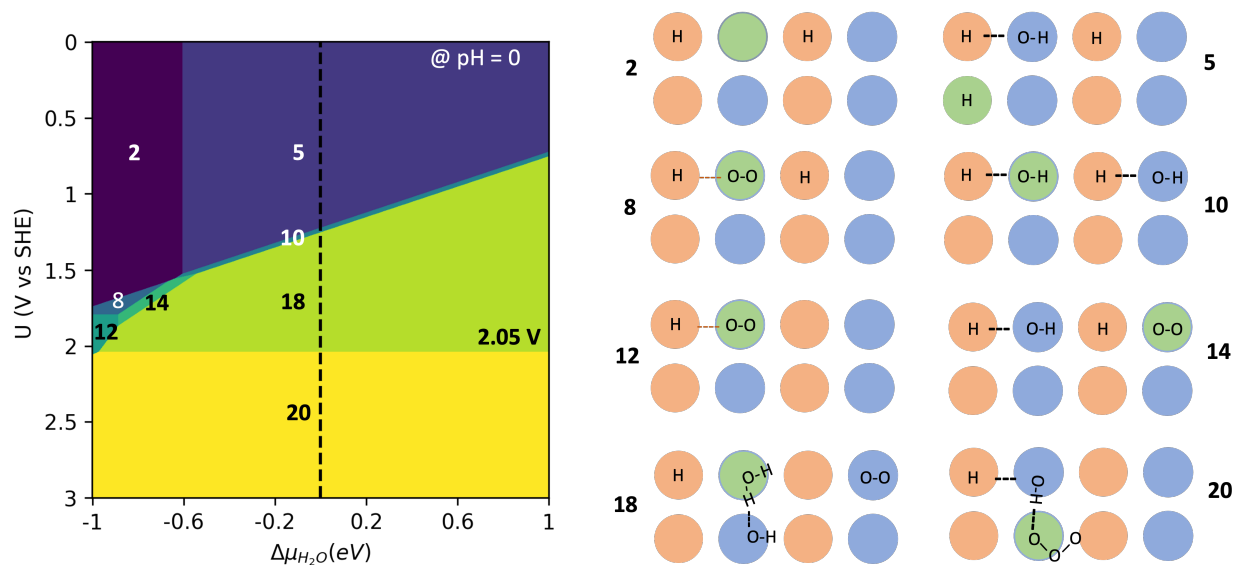

Figure 2: An electrochemical phase diagram representing the stability of different atom configurations on an undoped pristine $SnO_2(110)$ surface as a function of chemical potential of water, μ_{H_2O}, and applied potential at pH = 0. On the right, surface structures are depicted using orange dots that represent bridging oxygen sites and blue dots represent tin active sites on $SnO_2(110)$.

Figure 3: An electrochemical phase diagram representing the stability of different atom configurations on a Ni-doped $SnO_2(110)$ surface as a function of chemical potential of water, μ_{H_2O}, and applied potential at pH = 0. On the right, the surface structures are depicted using orange dots that represent bridging oxygen sites, blue dots represent tin active sites, and green dots represent the Ni dopant on $SnO_2(110)$.

From Figure 3, the limiting potential was calculated to be 2.05 V at standard conditions. The phase diagram also indicates that the most stable structure leading up to zone formation is O_2* with two co-adsorbed water molecules, and the limiting potential for reacting this state into O_3* with one co-adsorbed water is lowered from 2.22 V on the pristine surface to 2.05 V on the Ni-doped surface. This is the first indication we have been able to observe from computational DFT studies that Ni-doping would result in lower overpotentials for EOP.

To summarize this phase diagram analysis, there are several key points.

1) Effectively all of the thermodynamically relevant adsorbate structures for EOP at all considered potentials involve some degree of dissociated water coadsorbed on the surface. Thus, computational efforts that do not include energy contributions to co-adsorbed water might not be providing physically consistent predictions of reaction energies.

2) In general, electrochemical phase diagrams converge to the conclusion that the O_2* intermediate (structure 18) is the most thermodynamically stable prior to catalytic formation of ozone. Thus, either stabilizing the energy of O_3* with respect to O_2* via doping or

14

finding other mechanistic routes to O_3* that eschew O_2* (perhaps via solution phase radical reactions) appear to be paths forward to more energetically efficient EOP catalysts.

We reiterate that this phase diagram only shows the role of dopants from a thermodynamic perspective, but it does not include insights on kinetic energy barriers of the reaction steps (which require significantly more time and effort to identify). Future work on this topic would ideally consider kinetic energy barriers involving LOM, AEM for surface catalytic reaction mechanisms. It remains to be seen if computational quantum chemistry methods such as DFT would be suitable for this, or whether modern atomistic reactive forcefields might be more appropriate.

Conclusions and Outlook

We have used computational quantum chemistry to gain physical insights into the surface catalytic reaction pathway including AEM and LOM steps for EOP. The primary messages we make are

1. EOP intermediates are strongly stabilized by the presence of dissociated water molecules that more simplistic computational modeling might not consider.

2. Accounting for dissociated water interactions via electrochemical phase diagrams provides a mechanistic picture that is in agreement with experimental observations that were not possible with standard CHE modeling of sequential EOP steps.

3. Differentiation between AEM and LOM mechanisms is challenged at this time since predictive computational models should ideally account for explicit water beyond levels we were able to in this study.

Our results help us predict that catalysts that would stabilize the computationally observed O_3* intermediate relative to the computationally observed O_2* intermediate would be a valid route for improving the efficiencies of EOP catalysis on NATO and/or other doped

15

systems based on SnO_2. However, it is presently unclear if these insights would be transferrable to other electrocatalysts that appear to exhibit notably different characteristics, *e.g.* PbO_2. Indeed, isotope studies on PbO_2 indicated that substantial amounts of lattice oxygens appear in O_3 products, and so a LOM pathway was considered a favored pathway over the AEM.[17] On the other hand, our own isotope studies on NATO indicate that observed EOP activity is likely due to a competition between multiple active pathways including LOM, AEM, and well as non-catalytic corrosion that involves solution phase radicals.[49] Thus, there is evidence that EOP mechanisms on NATO will not be the same as EOP mechanisms on PbO_2, the oxygen vacancy formation energies and stabilities of these materials are not the same, however understanding both in tandem would likely provide valuable perspectives for advancing EOP catalysis.

In closing, future efforts in elucidating electrocatalytic processes will ideally include more predictive modeling that accounts for multiple oxide surface facets, dopants, explicit waters, solution phase radicals, and kinetic barriers of parallel AEM, LOM, and corrosion, all simultaneously. Doing so with standard DFT modeling is expected to be challenging into the future, but this presents opportunities for more reactive forcefields developments that would be suitable for identifying complex atomic scale mechanisms in electrochemical environments.[50–53]

Acknowledgement

work used the H2P cluster, which is supported by NSF award number OAC-2117681.

Supporting Information Available

- A PDF file of supporting information of DFT calculations.

- A json archive of calculation files.

References

(1) Peleg, M. The chemistry of ozone in the treatment of water. *Water Research* **1976**, *10*, 361–365.

(2) Mohammadi, Z.; Shalavi, S.; Soltani, M. K.; Asgary, S. A Review of the Properties and Applications of Ozone in Endodontics: An Update. *Iranian Endodontic Journal* **2013**, *8*, 40.

(3) Rakness, K. L. Ozone in drinking water treatment : process design, operation, and optimization. **2005**,

(4) Christensen, P. A.; Yonar, T.; Zakaria, K. The Electrochemical Generation of Ozone: A Review. *Ozone: Science and Engineering* **2013**, *35*, 149–167.

(5) Kraft, A. Electrochemical Water Disinfection: A Short Review. *Platinum Metals Review* **2008**, *52*, 177–185.

(6) Okada, F.; Tanaka, S.; Tanaka, S.; Naya, K. Electrochemical Production of 70 wt ppm Ozone Water. *Electrochimica Acta* **2015**, *153*, 210–216.

(7) Marini, S.; Salvi, P.; Nelli, P.; Pesenti, R.; Villa, M.; Berrettoni, M.; Zangari, G.; Kiros, Y. Advanced alkaline water electrolysis. *Electrochimica Acta* **2012**, *82*, 384–391.

(8) Zeng, K.; Zhang, D. Recent progress in alkaline water electrolysis for hydrogen production and applications. *Progress in Energy and Combustion Science* **2010**, *36*, 307–326.

(9) Rossmeisl, J.; Logadottir, A.; Nørskov, J. K. Electrolysis of water on (oxidized) metal surfaces. *Chemical Physics* **2005**, *319*, 178–184.

(10) Rossmeisl, J.; Qu, Z. W.; Zhu, H.; Kroes, G. J.; Nørskov, J. K. Electrolysis of water on oxide surfaces. *Journal of Electroanalytical Chemistry* **2007**, *607*, 83–89.

(11) Man, I. C.; Su, H. Y.; Calle-Vallejo, F.; Hansen, H. A.; Martínez, J. I.; Inoglu, N. G.; Kitchin, J.; Jaramillo, T. F.; Nørskov, J. K.; Rossmeisl, J. Universality in Oxygen Evolution Electrocatalysis on Oxide Surfaces. *ChemCatChem* **2011**, *3*, 1159–1165.

(12) Zagalskaya, A.; Alexandrov, V. Role of Defects in the Interplay between Adsorbate Evolving and Lattice Oxygen Mechanisms of the Oxygen Evolution Reaction in RuO2 and IrO2. *ACS Catalysis* **2020**, *10*, 3650–3657.

(13) Amadelli, R.; De Battisti, A.; Girenko, D. V.; Kovalyov, S. V.; Velichenko, A. B. Electrochemical oxidation of trans-3,4-dihydroxycinnamic acid at PbO2 electrodes: Direct electrolysis and ozone mediated reactions compared. *Electrochimica Acta* **2000**, *46*, 341–347.

(14) Christensen, P. A.; Lin, W. F.; Christensen, H.; Imkum, A.; Jin, J. M.; Li, G.; Dyson, C. M. Room Temperature, Electrochemical Generation of Ozone with 50%Current Efficiency in 0.5M Sulfuric Acid at Cell Voltages 3V. *Ozone: Science & Engineering* **2009**, *31*, 287–293.

(15) Wang, Y.-H.; Chen, Q.-Y. Anodic Materials for Electrocatalytic Ozone Generation. *International Journal of Electrochemistry* **2013**, *2013*, 1–7.

(16) Gibson, G.; Wang, Z.; Hardacre, C.; Lin, W. F. Insights into the mechanism of electro-

18

chemical ozone production via water splitting on the Ni and Sb doped SnO 2 catalyst. *Physical Chemistry Chemical Physics* **2017**, *19*, 3800–3806.

(17) Jiang, W.; Wang, S.; Liu, J.; Zheng, H.; Gu, Y.; Li, W.; Shi, H.; Li, S.; Zhong, X.; Wang, J. Lattice oxygen of PbO2 induces crystal facet dependent electrochemical ozone production. *Journal of Materials Chemistry A* **2021**, *9*, 9010–9017.

(18) Panizza, M.; Cerisola, G. Application of diamond electrodes to electrochemical processes. *Electrochimica Acta* **2005**, *51*, 191–199.

(19) Honda, Y.; Ivandini, T. A.; Watanabe, T.; Murata, K.; Einaga, Y. An electrolyte-free system for ozone generation using heavily boron-doped diamond electrodes. *Diamond and Related Materials* **2013**, *40*, 7–11.

(20) Awad, M. I.; Saleh, M. M. Electrochemical generation of ozone at PbO2-loaded platinum screens. *Journal of Solid State Electrochemistry* **2010**, *14*, 1877–1883.

(21) De Sousa, L. G.; Franco, D. V.; Da Silva, L. M. Electrochemical ozone production using electrolyte-free water for environmental applications. *Journal of Environmental Chemical Engineering* **2016**, *4*, 418–427.

(22) Rahmani, A. R.; Azarian, G.; Nematollahi, D. New insights into electrocatalytic ozone generation using Pt/Ni-Sb-SnO2 and GC/Ni-Sb-SnO2 electrodes. *Journal of Electroanalytical Chemistry* **2018**, *824*, 216–225.

(23) Lansing, J. L.; Zhao, L.; Siboonruang, T.; Attanayake, N. H.; Leo, A. B.; Fatouros, P.; Park, S. M.; Graham, K. R.; Keith, J. A.; Tang, M. Gd-Ni-Sb-SnO2 electrocatalysts for active and selective ozone production. *AIChE Journal* **2021**, *67*.

(24) Wang, Y.-H.; Cheng, S.; Chan, K.-Y.; Li, X. Y. Electrolytic Generation of Ozone on Antimony- and Nickel-Doped Tin Oxide Electrode. *Journal of The Electrochemical Society* **2005**, *152*, D197.

(25) Christensen, P. A.; Zakaria, K.; Curtis, T. P. Structure and Activity of Ni- and Sb–doped SnO2 Ozone Anodes. *Ozone: Science & Engineering* **2012**, *34*, 49–56.

(26) Christensen, P. A.; Zakaria, K.; Christensen, H.; Yonar, T. The Effect of Ni and Sb Oxide Precursors, and of Ni Composition, Synthesis Conditions and Operating Parameters on the Activity, Selectivity and Durability of Sb-Doped SnO 2 Anodes Modified with Ni . *Journal of The Electrochemical Society* **2013**, *160*, H405–H413.

(27) Christensen, P. A.; Attidekou, P. S.; Egdell, R. G.; Maneelok, S.; Manning, D. A. C.; Palgrave, R. Identification of the Mechanism of Electrocatalytic Ozone Generation on Ni/Sb-SnO2. *The Journal of Physical Chemistry C* **2017**, *121*, 1188–1199.

(28) Sandin, S.; Cheritat, A.; Bäckström, J.; Cornell, A. Deposition efficiency in the preparation of ozone-producing nickel and antimony doped tin oxide anodes. *Journal of Electrochemical Science and Engineering* **2017**, *7*, 51–64.

(29) Shanthi, E.; Dutta, V.; Banerjee, A.; Chopra, K. L. Electrical and optical properties of undoped and antimony-doped tin oxide films. *Journal of Applied Physics* **1980**, *51*, 6243–6251.

(30) Zhang, Y.; Yang, Y.; Yang, S.; Quispe-Cardenas, E.; Hoffmann, M. R. Application of Heterojunction Ni-Sb-SnO2 Anodes for Electrochemical Water Treatment. *ACS ES and T Engineering* **2021**, *1*, 1236–1245.

(31) Li, W.; Feng, G.; Wang, S.; Liu, J.; Zhong, X.; Yao, Z.; Deng, S.; Wang, J. Lattice Oxygen of PbO2(101) Consuming and Refilling via Electrochemical Ozone Production and H2O Dissociation. *Journal of Physical Chemistry C* **2022**, *126*, 8627–8636.

(32) Kresse, G.; Hafner, J. Ab initio molecular dynamics for liquid metals. *Physical Review B* **1993**, *47*, 558–561.

(33) Kresse, G.; Furthmüller, J. Efficient iterative schemes for ab initio total-energy calculations using a plane-wave basis set. *Physical Review B - Condensed Matter and Materials Physics* **1996**, *54*, 11169–11186.

(34) Hutchinson, M.; Widom, M. VASP on a GPU: Application to exact-exchange calculations of the stability of elemental boron. *Computer Physics Communications* **2012**, *183*, 1422–1426.

(35) Hacene, M.; Anciaux-Sedrakian, A.; Rozanska, X.; Klahr, D.; Guignon, T.; Fleurat-Lessard, P. Accelerating VASP electronic structure calculations using graphic processing units. *Journal of Computational Chemistry* **2012**, *33*, 2581–2589.

(36) Perdew, J. P.; Burke, K.; Ernzerhof, M. Generalized gradient approximation made simple. *Physical Review Letters* **1996**, *77*, 3865–3868.

(37) Blöchl, P. E. Projector augmented-wave method. *Physical Review B* **1994**, *50*, 17953–17979.

(38) Groenenboom, M. C.; Anderson, R. M.; Horton, D. J.; Basdogan, Y.; Roeper, D. F.; Policastro, S. A.; Keith, J. A. Doped Amorphous Ti Oxides to Deoptimize Oxygen Reduction Reaction Catalysis. *Journal of Physical Chemistry C* **2017**, *121*, 16825–16830.

(39) Türk, H.; Götsch, T.; Schmidt, F. P.; Hammud, A.; Ivanov, D.; de Haart, L. G.; Vinke, I. C.; Eichel, R. A.; Schlögl, R.; Reuter, K.; Knop-Gericke, A.; Lunkenbein, T.; Scheurer, C. Sr Surface Enrichment in Solid Oxide Cells – Approaching the Limits of EDX Analysis by Multivariate Statistical Analysis and Simulations. *ChemCatChem* **2022**, *14*, e202200300.

(40) Linstrom, P. J.; Mallard, W. G. The NIST Chemistry WebBook: A chemical data resource on the Internet. *Journal of Chemical and Engineering Data* **2001**, *46*, 1059–1063.

(41) Keith, J. A.; Carter, E. A. Quantum chemical benchmarking, validation, and prediction of acidity constants for substituted pyridinium ions and pyridinyl radicals. *Journal of Chemical Theory and Computation* **2012**, *8*, 3187–3206.

(42) Nørskov, J. K.; Rossmeisl, J.; Logadottir, A.; Lindqvist, L.; Kitchin, J. R.; Bligaard, T.; Jónsson, H. Origin of the Overpotential for Oxygen Reduction at a Fuel-Cell Cathode. *The Journal of Physical Chemistry B* **2004**, *108*, 17886–17892.

(43) Griego, C. D.; Maldonado, A. M.; Zhao, L.; Zulueta, B.; Gentry, B. M.; Lipsman, E.; Choi, T. H.; Keith, J. A. Computationally Guided Searches for Efficient Catalysts through Chemical/Materials Space: Progress and Outlook. *The Journal of Physical Chemistry C* **2021**, *125*, 6495–6507.

(44) Reuter, K.; Scheffler, M. First-Principles Atomistic Thermodynamics for Oxidation Catalysis: Surface Phase Diagrams and Catalytically Interesting Regions. *Physical Review Letters* **2003**, *90*, 4.

(45) Exner, K. S.; Anton, J.; Jacob, T.; Over, H. Chlorine Evolution Reaction on RuO2(110): Ab initio Atomistic Thermodynamics Study - Pourbaix Diagrams. *Electrochimica Acta* **2014**, *120*, 460–466.

(46) Saravanan, K.; Basdogan, Y.; Dean, J.; Keith, J. A. Computational investigation of CO2 electroreduction on tin oxide and predictions of Ti, V, Nb and Zr dopants for improved catalysis. *Journal of Materials Chemistry A* **2017**, *5*, 11756–11763.

(47) Santarossa, G.; Hahn, K.; Baiker, A. Free energy and electronic properties of water adsorption on the SnO 2(110) Surface. *Langmuir* **2013**, *29*, 5487–5499.

(48) Kanan, D. K.; Keith, J. A.; Carter, E. A. Water adsorption on MnO:ZnO(001) — From single molecules to bilayer coverage. *Surface Science* **2013**, *617*, 218–224.

(49) Alaufey, R.; Zhao, L.; Lindsay, A.; Siboonruang, T.; Wu, Q.; Keith, J. A.; Wood, E.; Tang, M. Interplay of catalyst corrosion and homogeneous reactive oxygen species in electrochemical ozone production. *ChemRxiv.* **2023**,

(50) Senftle, T. P.; Hong, S.; Islam, M. M.; Kylasa, S. B.; Zheng, Y.; Shin, Y. K.; Junkermeier, C.; Engel-Herbert, R.; Janik, M. J.; Aktulga, H. M.; Verstraelen, T.; Grama, A.; Van Duin, A. C. The ReaxFF reactive force-field: development, applications and future directions. *npj Computational Materials 2016 2:1* **2016**, *2*, 1–14.

(51) Lindsey, R. K.; Fried, L. E.; Goldman, N. ChIMES: A Force Matched Potential with Explicit Three-Body Interactions for Molten Carbon. *Journal of Chemical Theory and Computation* **2017**, *13*, 6222–6229.

(52) Mishra, R. K.; Mohamed, A. K.; Geissbühler, D.; Manzano, H.; Jamil, T.; Shahsavari, R.; Kalinichev, A. G.; Galmarini, S.; Tao, L.; Heinz, H.; Pellenq, R.; van Duin, A. C.; Parker, S. C.; Flatt, R. J.; Bowen, P. cemff: A force field database for cementitious materials including validations, applications and opportunities. *Cement and Concrete Research* **2017**, *102*, 68–89.

(53) Unke, O. T.; Chmiela, S.; Sauceda, H. E.; Gastegger, M.; Poltavsky, I.; Schütt, K. T.; Tkatchenko, A.; Müller, K. R. Machine learning force fields. *Chem. Rev.* **2021**, *121*, 10142–10186.

TOC Graphic